Current Research in Neurobiology 7 (2024) 100138

Contents lists available at ScienceDirect

Current Research in Neurobiology

journal homepage: www.sciencedirect.com/journal/current-research-in-neurobiology

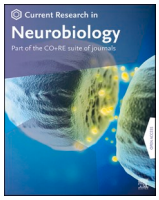

Analysis of the neuromuscular deficits caused by STAM1 deficiency

John W. McLean [a,2,1], Mary VanHart [a,1], Madilyn P. McWilliams [a], Charlene B. Farmer [b], David K. Crossman [c], Rita M. Cowell [b], Julie A. Wilson [a], Scott M. Wilson [a,*]

[a] Department of Neurobiology, Evelyn F. McKnight Brain Institute, Civitan International Research Center, University of Alabama at Birmingham, Birmingham, 35294, Alabama, USA
[b] Department of Neurology, University of Alabama at Birmingham, Birmingham, AL, 35294, USA
[c] Department of Human Genetics, University of Alabama at Birmingham, Birmingham, AL, 35294, USA

ARTICLE INFO

Keywords:
ESCRT-0
Ubiquitin
HGS
STAM1
Endosome
Synapse and NMJ

ABSTRACT

The endosomal sorting complexes required for transport (ESCRT) pathway is composed of a series of protein complexes that are essential for sorting cargo through the endosome. In neurons, the ESCRT pathway is a key mediator of many cellular pathways that regulate neuronal morphogenesis as well as synaptic growth and function. The ESCRT-0 complex, consisting of HGS (hepatocyte growth factor-regulated tyrosine kinase substrate) and STAM (signal-transducing adaptor molecule), acts as a gate keeper to this pathway, ultimately determining the fate of the endosomal cargo. We previously showed that a single nucleotide substitution in *Hgs* results in structural and functional changes in the nervous system of *teetering* mice. To determine if these changes occurred as a function of HGS's role in the ESCRT pathway and its association with STAM1, we investigated if STAM1 deficiency also leads to a similar impairment of the nervous system. In contrast to *teetering* mice that die within 5 weeks of age and exhibit reduced body mass, 1-month-old *Stam1* knockout mice were not visibly different from controls. However, by 3 months of age, STAM1 deficiency caused reduced muscle mass, strength, and motor performance. These changes in motor function did not correlate with either a loss in motor neuron number or abnormal myelination of peripheral nerves. Instead, the motor endplate structure was altered in the *Stam1* knockout mice by 1 month of age and continued to degenerate over time, correlating with a significant reduction in muscle fiber size and increased expression of the embryonic γ acetylcholine receptor (AChR) subunit at 3 months of age. There was also a significant reduction in the levels of two presynaptic SNARE proteins, VTI1A and VAMP2, in the motor neurons of the *Stam1* knockout mice. As loss of STAM1 expression replicates many of the structural changes at the motor endplates that we have previously reported with loss of HGS, these results suggest that the HGS/STAM1 complex plays a critical role in maintaining synaptic structure and function in the mammalian nervous system.

1. Introduction

Proteins accumulate damage during their lifespan and need to be degraded and replaced in order to effectively maintain cellular processes. The maintenance of the cellular proteome is especially crucial in post-mitotic cells such as neurons, as defects in the clearance of damaged proteins are observed in many neurological diseases (Tseng et al., 2023). The two major degradative pathways are the ubiquitin-proteasome system and the autophagy/endolysosomal system. Understanding the mechanisms regulating these pathways has been an area of intense research since aberrant protein homeostasis disrupts many cellular pathways.

Deficits in the endolysosomal pathway are thought to contribute to pathogenesis of Parkinson's disease, amyotrophic lateral sclerosis and other neurodegenerative diseases (Schreij et al., 2016; Toupenet Marchesi et al., 2021; Smith et al., 2022; Diab et al., 2023). Substrates for the endolysosomal pathway include internalized cell surface receptors that are sorted through the endocytic pathway, misfolded cytoplasmic proteins that are identified by chaperone-mediated autophagy, and cellular organelles that are engulfed by autophagosomes

* Corresponding author. 1825 University Blvd., SHEL 914, Birmingham, AL, 35294, USA.
E-mail address: livvy01@uab.edu (S.M. Wilson).
[1] Co-first authors.
[2] Present address: Graduate Interdisciplinary Program in Neuroscience, University of Arizona, Tucson, Arizona 85721, United States of America.

https://doi.org/10.1016/j.crneur.2024.100138
Received 23 February 2024; Received in revised form 17 July 2024; Accepted 20 August 2024
Available online 23 August 2024

(Jackson and Hewitt, 2016). The sorting of internalized cell surface proteins to the lysosome requires the action of the ESCRT pathway, which is composed of four complexes (ESCRT-0, -I, -II and -III) (Hurley, 2008). These complexes act in a sequential manner to form multivesicular bodies which eventually fuse with lysosomes. Mutations in the ESCRT-0 protein HGS and the ESCRT-related protein CHMP2B have been shown to cause neurodegeneration in mouse models, and familial forms of amyotrophic lateral sclerosis (Parkinson et al.) and frontotemporal dementia are linked to mutations in CHMP2B (Skibinski et al., 2005; Parkinson et al., 2006). While there is emerging evidence of a critical role for the ESCRT pathway in neuronal proteostasis (Watson et al., 2015; Sheehan et al., 2016; Sheehan and Waites, 2019; Birdsall et al., 2022), little is known about how individual ESCRT components function in the nervous system.

We previously reported that the neurological deficits observed in the spontaneously occurring *teetering* mouse were due to a mutation in HGS (Watson et al., 2015). The *teetering* mice display muscle weakness, reduced muscle size and early perinatal lethality by 5 weeks of age. These changes in muscle function are accompanied by both structural and functional alterations at the neuromuscular junction (NMJ) (Watson et al., 2015). Mechanistic *in vitro* studies are consistent with these findings and support a role for HGS in the regulation of synaptic vesicle membrane proteins (Uytterhoeven et al., 2011; Sheehan et al., 2016). We also showed that HGS expression in Schwann cells is required for sciatic nerve myelination and for the endosomal sorting of the ERBB2/3 receptors (McLean et al., 2022). Although these findings indicate that HGS is required for multiple aspects of nervous system function, it is not known if the neuromuscular defects resulting from HGS deficiency are due to impaired ESCRT-0 activity or to loss of HGS functions that are independent of its association with STAM, the other member of the ESCRT-0 complex (Hurley, 2008; Rusten et al., 2011).

The ESCRT-0 complex identifies cargo that is to be sorted through the endolysosomal pathway and sequesters it on the surface of endosomal membranes (Bilodeau et al., 2002; Babst, 2005). Previous studies in mice demonstrated that a constitutive deletion of *Stam1* results in loss of hippocampal CA3 pyramidal neurons at 5 weeks of age, but the effects of loss of STAM1 on either protein homeostasis or the peripheral nervous system were not assessed (Yamada et al., 2001). To determine if STAM1 deficiency is sufficient to cause similar neuromuscular defects as seen in the HGS-deficient *teetering* mice, we investigated the impact of the knockout mutation of *Stam1* (*Stam1*^{KO}) on motor function, myelination, motor neuron viability, and NMJ structure. While *Stam1*^{KO} mice did not exhibit signs of motor dysfunction at 1 month, we observed significant decreases in muscle mass and muscle strength by 3 months of age. These defects were not associated with a loss of lower motor neurons, but there was an increase in markers of reactive astrocytes in the spinal cords of 3-month-old *Stam1*^{KO} mice. In contrast to the critical role HGS plays in peripheral nerve myelination in the *teetering* mice (Watson et al., 2015), STAM1 was not required for myelination of the peripheral nerves. However, there was progressive neurodegeneration of motor endplates, as determined by the presence of ultra-terminal swellings, sproutings, and denervated terminals, in the gastrocnemius muscles of the *Stam1*^{KO} mice. Consistent with impaired motor endplate structure, we found aberrant levels of acetylcholine receptors (AChRs) in the *Stam1*^{KO} mice, and the size of the muscle fibers was significantly reduced compared to controls. Absence of STAM1 also resulted in reduced levels of the presynaptic proteins VTI1A and VAMP2. These findings demonstrate that, like HGS, STAM1 expression is necessary for synapse stability at the NMJ.

2. Materials and methods

2.1. Animals

All research complied with the United States Animal Welfare Act and other federal statutes and regulations relating to animals and experiments involving animals and adhered to principles stated in the United States National Research Council Guide for the Care and Use of Laboratory Animals. Experiments were conducted in accordance with UAB IACUC animal protocol 20457. Mice were housed at the University of Alabama at Birmingham, which is fully accredited by the Association for Assessment and Accreditation of Laboratory Animal Care International (A3255-01). Mice were maintained with a 12 h light (0700 EDT)/12 h dark cycle (1900 EDT) in Thoren racks with forced air ventilation. Plastic cages were 19.56 × 30.91 × 13.31 cm and contained 2 cm of hard wood chip bedding (Northeastern Products, Warrensburg, NY). Mice were given ad libitum access to food (LabDiet, St. Louis, MO) and water. Offspring of identical sex were separated at 3 weeks of age and housed in cages at a maximum density of 5 mice/cage. Mice were assigned numbers, ear punched for identification, and genotyped using DNA obtained by tail clipping. Equal numbers of 1- and 3-month-old male and female animals were used for each genotype in these experiments.

Mice with the *Stam1*^{tm1Sug} allele on the BALB/c background were initially purchased from RIKEN Biosource Research Center (Koyadai, Japan, Stock RBRC00672). These mice were backcrossed to C57BL/6J mice (Jackson Laboratory, Bar Harbor, MA, Stock 000664) for 10 generations before being used to generate the *Stam1* knockout mice (hereafter referred to as *Stam1*^{KO}) used in these studies. Immunoblot analysis confirmed the absence of any detectable STAM1 expression in the *Stam1*^{KO} mice. Wild-type controls and *Stam1*^{KO} mice were generated by breeding *Stam1*$^{KO/+}$ heterozygotes. The *Thy1-Yfp* mouse line (B6.Cg-Tg (Thy1-YFP)16Jrs/J, Jackson Laboratory Stock 003709) was crossed into the *Stam1*^{KO} mouse line for imaging NMJs and spinal cord motor neurons.

2.2. Body and muscle wet weight analysis

Gastrocnemius muscles were taken from 1- and 3-month-old wild-type and *Stam1*^{KO} mice. Muscle and body weights were collected from at least six animals per genotype, and the values are reported as the average muscle or body mass ± SEM.

2.3. Behavioral analysis

Motor and sensory performance were evaluated at both 1 and 3 months of age with wild-type and *Stam1*^{KO} mice. Before each behavioral assay, the animal was allowed to habituate to the testing room for 30 min. Unpaired Student's t-tests were performed to determine the significance of the data.

Animals were handled at least two days prior to open field testing. On the day of testing, mice were placed in an open field arena (43 × 43 × 30-cm Plexiglas box) and activity was measured for 5 min by photo beam detectors, then analyzed via ENV-515 software (Med Associates, St. Albans, VT). Coordination and balance were measured by placing mice on an accelerating rotarod (ENV-575, Med Associates) and recording the latency to fall.

The initial speed of the rotarod began at 3.5 rpm and then accelerated to 35 rpm during a 5 min period. Three trials a day were performed on each mouse, with a 15 min inter-trial rest period, for three consecutive days. The data for latency to fall is the average of the three daily averages for each mouse.

The Chatillon Ametek Force Gauge (Agawam, MA) was used to determine grip strength. The maximum force generated was recorded and each mouse trial consisted of 12 repetitions of the assay with the two highest and two lowest data points dropped from final analysis.

Before assessing sensory performance, each animal was further habituated in an open-gridded floor chamber for 10 min. Von Frey fibers ranging from 0.02 to 8 g of force (North Coast Medical, Gilroy, CA) were applied to the foot in ascending order beginning with the smallest fiber. Fibers were placed in the central region of the plantar surface so as to avoid the foot pads, and the threshold for hind paw withdrawal was determined.

2.4. Small molecule fluorescence in situ hybridization (FISH)

Mice (n = 3, 3-month-old males) were anesthetized with isoflurane prior to decapitation, the spinal column was removed, and the spinal cord was extruded with 1X PBS. Lumbar spinal cords were blocked, immediately frozen on dry ice, and stored at −80 °C until cryosectioning at 20 μm on a Leica CM 1860 cryostat and collection on SuperFrost Plus slides (Epredia, Kalamazoo, MI). Small molecule FISH was performed using the RNAscope Multiplex Fluorescent Assay (Advanced Cell Diagnostics, Newark, CA). Tissues were fixed with 4% paraformaldehyde (PFA) for 15 min, dehydrated in a series of 50%, 70%, and 100% ethanol solutions for 5 min each, and treated with PBS containing 0.3% hydrogen peroxide for 5 min and then protease III solution (Advanced Cell Diagnostics) for 5 min. Tissues were then incubated for 2 h at 40 °C in a mixture of probes recognizing *Chat* (Advanced Cell Diagnostics, Cat# 408731-C1), *Hgs* (Advanced Cell Diagnostics, Cat# 1215751-C2), and *Stam1* (Advanced Cell Diagnostics, Cat# 1215761-C3), followed by a series of amplification buffer steps (30 min, steps 1 and 2; 15 min, step 3) at 40 °C. Then, each probe was HRP-labeled sequentially with TSA-conjugated fluorescein, Cy3, and Cy5 respectively (Cat#: FP1168, FP1170, FP1171, PerkinElmer, Shelton, CT) for 30 min at 40 °C. Slides were coverslipped with Prolong Diamond Antifade Mountant with DAPI (Thermo Fisher Scientific, Waltham, MA), and images were captured with a Nikon Eclipse Ti2 and AX confocal system. Representative images are shown to demonstrate the neuroanatomical distribution of the transcripts.

2.5. Curation of publicly available transcriptional data in the mouse nervous system

Single-cell gene expression data, expression values and metadata per cluster files were downloaded from https://mousebrain.org and accessed using loomR version 0.2.0 (https://satijalab.org/loomR/loomR_tutorial.html). Categorization of cell clusters by type was guided by the classification of each cluster provided by the original study (Zeisel et al., 2018). Data are presented as abundance relative to the highest expressing cluster for each gene.

2.6. Quantitation of motor neuron number

Motor neuron quantitation was carried out by cutting transverse frozen lumbar spinal cord sections from four 3-month-old wild-type or *Stam1*^{KO} mice that transgenically expressed the yellow fluorescent protein in motor neurons (Burgess et al., 2016). Sections were also counterstained with DAPI. Twelve L4/5 sections per animal were quantitated to determine motor neuron numbers. Images were collected on a ZEISS LSM 800 confocal microscope (ZEISS International), and motor neuron cell bodies in the ventral horn were counted and analyzed for differences in cell number.

2.7. Transmission electron microscopy of sciatic nerves

Sciatic nerves were dissected from 3-month-old wild-type and *Stam1*^{KO} mice. Nerves were placed in 3% PFA and 2% glutaraldehyde (GA) in 0.2 M sodium cacodylate buffer for 1.5 h, washed in 0.2 M sodium cacodylate, and then post-fixed in 1% osmium tetroxide for 1 h in the dark. Nerves were then thoroughly washed with 0.2 M sodium cacodylate, dehydrated in a series of increasing acetone concentrations (50%, 75%, 90%, 95% and 100% x 4) for 10 min each and then equilibrated into resin (Electron Microscopy Sciences, Hatfield, IL) by first rotating overnight in a 1:1 epoxy:acetone solution. Samples were moved into fresh 100% epoxy for 2 h each. This was repeated two more times, and the samples were then baked overnight at 65 °C. A Leica EM-UC6 ultramicrotome (Buffalo Grove, IL) was used to generate ultra-thin sections which were then stained for contrast with uranyl acetate and lead citrate. Sciatic nerve images were collected using a FEI Tecnai T-12 electron microscope (Delmont, PA) with a Hamamatsu digital camera (Bridgewater, NJ).

2.8. Morphometric analysis of sciatic nerves

Images for morphometric analysis were collected from adjacent but non-overlapping fields to determine axonal number, myelin thickness, and axonal density. ImageJ software (NIH, Bethesda, MD) was used to quantify axon diameter and myelin thickness. To determine g-ratio, the axon diameter was divided by the myelin plus axon diameter. At least 100 axons were measured from two separate fields for each animal. Micrographs of sciatic nerves were taken at 470x and used to determine axon density of myelinated fibers. Micrographs collected at 1100x were used to determine g-ratios.

2.9. Quantitative PCR

Total RNA was isolated from tissues with RNA-STAT60 and reverse transcribed using the Superscript VILO cDNA synthesis kit (Thermo Fisher Scientific). Individual gene assays were acquired from Applied Biosystems for each of the analyzed RNAs. ΔΔCt values were generated using *AChRα* (Mm00431629_m1), *AChRβ* (Mm00680412_m1), *AChRδ* (Mm00445545_m1), *AChrγ* (Mm00437419_m1) and *AChRε* (Mm00437411_m1). Taqman gene assays with *Actb* (Mm00607939_s1) served as an internal standard. qPCR results are shown as the average of two different amplifications of cDNAs that were generated from at least three different mice. Unpaired Student's t tests were conducted on ΔΔCt values from each genotype to determine their significance.

2.10. Isolation of proteins

Mice of appropriate age and genotype were deeply anesthetized via isoflurane prior to rapid decapitation. Tissues were removed and homogenized in a modified RIPA buffer containing 50 mM Tris, pH 7.5, 150 mM NaCl, 5 mM $MgCl_2$, 0.5 mM EGTA, 1 mM EDTA, 0.5% SDS, 1% Triton X-100, and 1% sodium deoxycholate. Complete protease inhibitors (Roche, Indianapolis, IN) and phosphatase inhibitor cocktail I (Sigma Aldrich, St. Louis, MO) were added to the homogenization buffer. After homogenization, tissues were centrifuged at 17 000×*g* for 10 min at 4 °C to remove insoluble material, and supernatants were removed and immediately frozen at −20 °C. Protein concentrations were determined using the bicinchoninic acid (BCA) protein assay kit from Pierce (Rockford, IL). Samples were then diluted in Laemmli buffer and heated to 100 °C for 5 min.

2.11. Immunoblot analysis

Proteins were resolved on NuPAGE 4–12% Bis-Tris gels (Life Technologies) and transferred onto nitrocellulose membranes. All primary antibodies (1:1000) and anti-mouse or anti-rabbit HRP conjugated secondary antibodies (1:6000) (cat. # 4050) Southern Biotechnology Associates, Birmingham, AL) were diluted in either 5% nonfat milk or 0.2% bovine serum albumin (BSA) in Tris-buffered saline with 1% Tween-20. Immunoblots were probed for TSG101(cat. # sc-7964), VPS36 (cat. # sc-79930), RAB3 (cat. # sc-136050), MAPT (cat. # sc-32274), PRNP (cat. # sc-69896), and SNAP25 (cat. # sc-7538) from Santa Cruz (Dallas, TX), APPL1 (cat. # 3858), LAMP2A (cat. # 9091), MAP1LC3A (cat. # 12741), EEA1 (cat. # 3288), RAB5 (cat. # 3547), RAB7 (cat. # 9367), RAB11 (cat. # 5589), ERBB2 (cat. # 2165), ERBB3 (cat. # 12709), ERBB4 (cat. # 4795), GRIA1 (cat. # 13185), AKT (cat. # 9272), pAKT308 (cat. # 13038), ERK (cat. # 9201), pERK (cat. # 4370), JNK (cat. # 9252), pJNK (cat. # 4668), GSK3β (cat. # 9315), pGSK3β (cat. # 5585), HGS (cat. # 15087), STAM1 (cat. # 13053), CLTC (cat. # 4796), STX6 (cat. # 2869), SYN1 (cat. # 5297), VAMP1 (cat. # 13151), VAMP2 (cat. # 13508), and VTI1A (cat. # 14764) from Cell Signaling Technologies (Danvers, MA), ALIX (cat. # MA5-32773), M6PR (cat. # PA5-

111123) and SYP (cat. # MA5-14532) from Thermo Fisher Scientific, CXCR4 (cat. # 11073-2-AP) from ProteinTech (Rosemount, IL), NTRK2 (cat. # AB_310445), EGFR (cat. # 06–847) from MilliporeSigma (Burlington, MA), SYT1 (cat. # 105 008), STX1A (cat. # 110 302) and STX1B (cat. # 110 402) from Synaptic Systems (Göttingen, Germany), and SV2A (cat. # SV2), ACTB (cat. # JLA20) and TUBB3 (cat. #E7) from Developmental Hybridoma Bank (Iowa City, IA). ACTB and TUBB3 were used as loading controls. Antibodies were visualized using SuperSignal West Pico Chemiluminescent Substrate (Thermo Fisher Scientific).

2.12. Quantitation of immunoblots

Blots were scanned using a Hewlett-Packard Scanjet 3970 (Palo Alto, CA) and quantitated using ImageJ software. Each value represents the mean and SEM from at least two blots using at least three different animals per genotype. Unpaired Student's t-tests were utilized to determine significant effects between genotypes.

2.13. Immunostaining and confocal microscopy

Whole mount immunostaining of tibialis anterior muscles was performed as previously described (Chen et al., 2009). Briefly, tibialis anterior muscles of 1- and 3-month-old wild-type and *Stam1*^{KO} mice (n = 3) containing the *Thy1-Yfp* transgene were dissected and immersed in ice-cold 2% PFA for 1 h. Muscles were then teased into bundles and transferred to 1% PFA in PBST (PBS + 1% Triton X-100) overnight at 4 °C with constant rocking. After staining with TRITC-labeled α-bungarotoxin (Thermo Fisher Scientific, B43451), samples were mounted, and images were acquired on a ZEISS LSM 800 confocal microscope. Endplate size was calculated by measuring the circumference of α-bungarotoxin-positive postsynaptic AChR clusters and computing the area with ImageJ software. Quantitation of axonal sprouts, swellings, and denervations was also performed using ImageJ software as previously described (Chen et al., 2009). At least 150 synapses were quantified from each mouse.

2.14. Immunostaining of spinal cord sections

L4/5 spinal cord sections fixed in either 4% PFA or Bouins fixative were cut at 10 μm and mounted onto Superfrost slides (Fisher Scientific). Sections were blocked in PBS containing 10% goat serum and 0.5% Triton X-100. Sections were then stained overnight with antibodies diluted at 1:100 for CC3 (CST 9661), IBA1 (CST 17198), EEA1 (CST, cat. # 3288) VTI1A (CST cat. # 14764), LAMP2A (CST cat. # 9091) or GFAP (cat #Z033429 Agilent, Santa Clara, CA), and primary antibodies were detected with either Alexa Fluor-488 (Thermo Fisher Scientific, cat. # A16123) or −568 (Thermo Fisher Scientific, cat. # 65–6111) labeled secondary antibodies. Secondary antibodies were diluted 1:1000 in blocking buffer. Digital images of IHC-stained L4/5 spinal cord sections were obtained at 40× magnification and acquired on a ZEISS LSM 800 confocal microscope. ImageJ software was used to determine the average fluorescence and number of puncta per motor neuron. Twelve sections per mouse, and a total of four mice per genotype, were analyzed to determine the fluorescence intensity of GFAP and IBA1.

2.15. Muscle H&E stain

Myofibril size was evaluated by cutting transverse frozen sections of gastrocnemius muscles from 1- and 3-month-old wild-type and *Stam1*^{KO} mice and staining with hematoxylin and eosin as described previously (Wang et al., 2017). Muscle fiber sizes were determined using ImageJ software.

2.16. Co-immunoprecipitation

Spinal cords from 1-month-old mice were homogenized in lysate buffer consisting of 10 mM Tris pH 7.2, 100 mM NaCl, 1 mM EDTA and 0.5% Triton X-100. Approximately 500 mg of lysate was incubated with a polyclonal STAM1 antibody (cat# 13053) overnight at 4 °C with constant rocking. The next day, protein A/G magnetic beads were washed three times with lysate buffer and then added to the antibody-protein solution. Antibody-bead complexes were allowed to form for 1 h at room temperature and then isolated using a magnetic block. Captured beads were then washed 3 times with lysate buffer. Proteins bound to the beads were isolated by adding 2X Laemmli buffer and then immunoblotted for STAM1, HGS and VTI1A.

2.17. Statistics

All statistical analysis was done in GraphPad Prism 8 (GraphPad Software, Boston, MA), using unpaired Student's t-tests to evaluate statistical significance, and data are presented as the average of biological replicates ± SEM. The Kolmogorov-Smirnov test was used to examine the statistical differences for size distribution of EEA1, LAMP2 and VTI1A puncta.

3. Results

3.1. Characterization of *Stam1*^{KO} mice

Because we wanted to be able to compare the neurological deficits of mice that are deficient in STAM1 with the HGS-deficient *teetering* mice, and genetic background can influence the phenotypic expression of a mutation, we first backcrossed mice with the *Stam1*^{tm1Sug} allele (Yamada et al., 2001), which was generated on a BALB/c background, onto wild-type C57BL/6J mice for ten generations. Homozygous *Stam1* knockout mice are referred to as *Stam1*^{KO} mice in this report. All experiments performed in this study compared wild-type mice to homozygous *Stam1*^{KO} mice. The *Stam1*^{KO} mice were born in a Mendelian manner, began to die around 4 months of age, and did not survive past 5 months of age (Fig. 1A). The survival plots are similar to those reported for the *Stam1*^{KO} allele on the BALB/c background (Yamada et al., 2001), indicating that the genetic background did not have a major effect on lifespan. Immunoblot analysis confirmed the absence of any detectable STAM1 expression in the *Stam1*^{KO} mice (Fig. 3A). Although the body and gastrocnemius muscle masses of the *Stam1*^{KO} mice were similar to controls at 1 month of age, both were significantly reduced in the *Stam1*^{KO} mice by 3 months of age (Fig. 1B and C). These results are similar to the effects reported for the *Stam1*^{KO} allele on the BALB/c genetic background (Yamada et al., 2001). Both genotypes also showed the expected sex-based difference in body mass and muscle mass that has previously been reported in mice (O'Reilly et al., 2021; Tsao et al., 2023). In an open field assay to examine overall motor function, the *Stam1*^{KO} mice displayed increased ambulatory time (Fig. 1D) and traveled significantly more (Fig. 1E) than controls at both 1 and 3 months of age but did not display any significant differences in their velocity (Fig. 1F). When rotarod and grip strength assays were used to examine motor function, the *Stam1*^{KO} mice showed significant impairment in motor performance at 3 months of age (Fig. 1G and H). Regardless of genotype, the males followed the trend in having increased grip-strength compared to females (Tsao et al., 2023). However, both male and female mice performed similarly in assays measuring ambulatory time, distance traveled, velocity, and motor coordination. The tactile sensitivity of the *Stam1*^{KO} mice, as measured by the von Frey assay, was also significantly reduced by 3 months of age (Fig. 1I). These results indicate that, similar to what we found for loss of HGS in the *teetering* mice, STAM1 is essential for both motor control and sensory function.

3.2. Spinal cord pathology due to loss of STAM1

The phenotypes observed in the *Stam1*^{KO} mice are similar to those found in other mouse models of neuromuscular disease which affect the

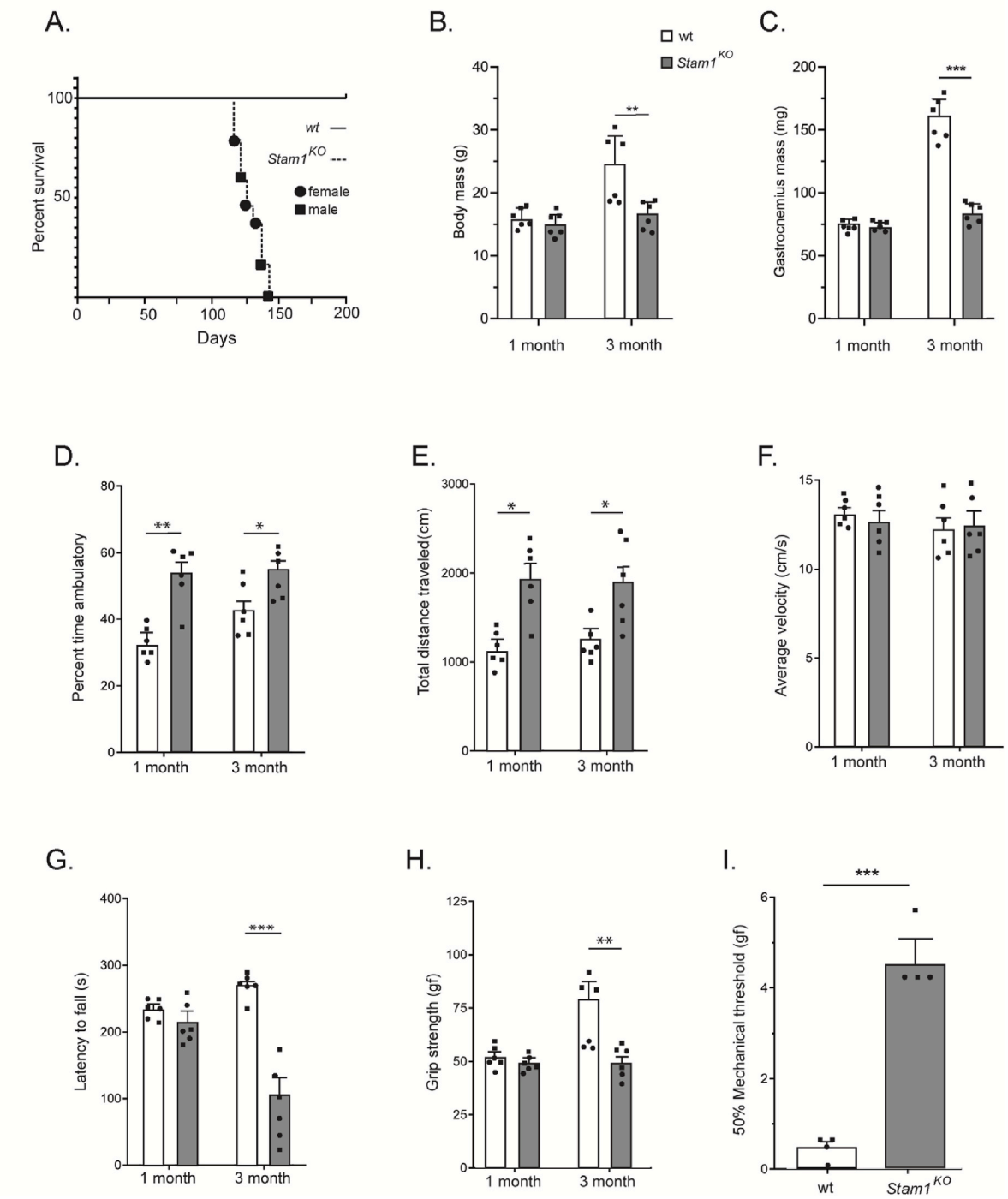

Fig. 1. Characterization of *Stam1*^{KO} mice. (A) Survival curves for wild-type (wt) and *Stam1*^{KO} mice. (B) Body mass (1 month p = 0.6502, 3 month p = 0.0027), (C) gastrocnemius mass (1 month p = 0.147, 3 month p = 0.0001), (D) percent time ambulatory in open field (1 month p = 0.0057, 3 month p = 0.0224), (E) distance traveled in open field (1 month p = 0.0117, 3 month p = 0.0274), (F) average velocity in open field (1 month p = 0.4394, 3 month p = 0.9742), (G) latency to fall (1 month p = 0.1771, 3 month p = 0.0001), and (H) fore-limb grip strength in grams force (gf) (1 month p = 0.3749, 3 month p = 0.0045) of wt and *Stam1*^{KO} mice. (I) Mechanical allodynia determined by von Frey assay (p = 0.0002) of 3-month-old wt and *Stam1*^{KO} mice. Data are shown as mean ± SEM, n = 6 mice per genotype for A-H and 4 for I. Open boxes indicate wt mice and grey boxes indicate *Stam1*^{KO} mice. Filled circles indicate female mice and filled squares represent male mice. *p < 0.05, **p < 0.01, ***p < 0.001.

survival of motor neurons, myelination of peripheral axons, or the stability of synaptic connections (Ripps et al., 1995; Wilson et al., 2002; Puls et al., 2003; Watson et al., 2015). To determine if a deficiency in STAM1 is likely to impair motor neurons by a cell-autonomous mechanism, we first examined if *Stam1* and *Hgs* are expressed in spinal cord motor neurons of wild-type mice using small molecule FISH (Fig. 2A–C). A FISH probe selective for choline acetyltransferase (*Chat*) mRNA was used to identify motor neurons in the ventral horn of the lumbar spinal cord. Fluorescence for both *Hgs* and *Stam1* mRNA was observed in cells throughout the spinal cord grey matter, with expression observed in *Chat*-positive cells with the morphology and location of ventral motor neurons (Fig. 2A). This distribution pattern is consistent with publicly

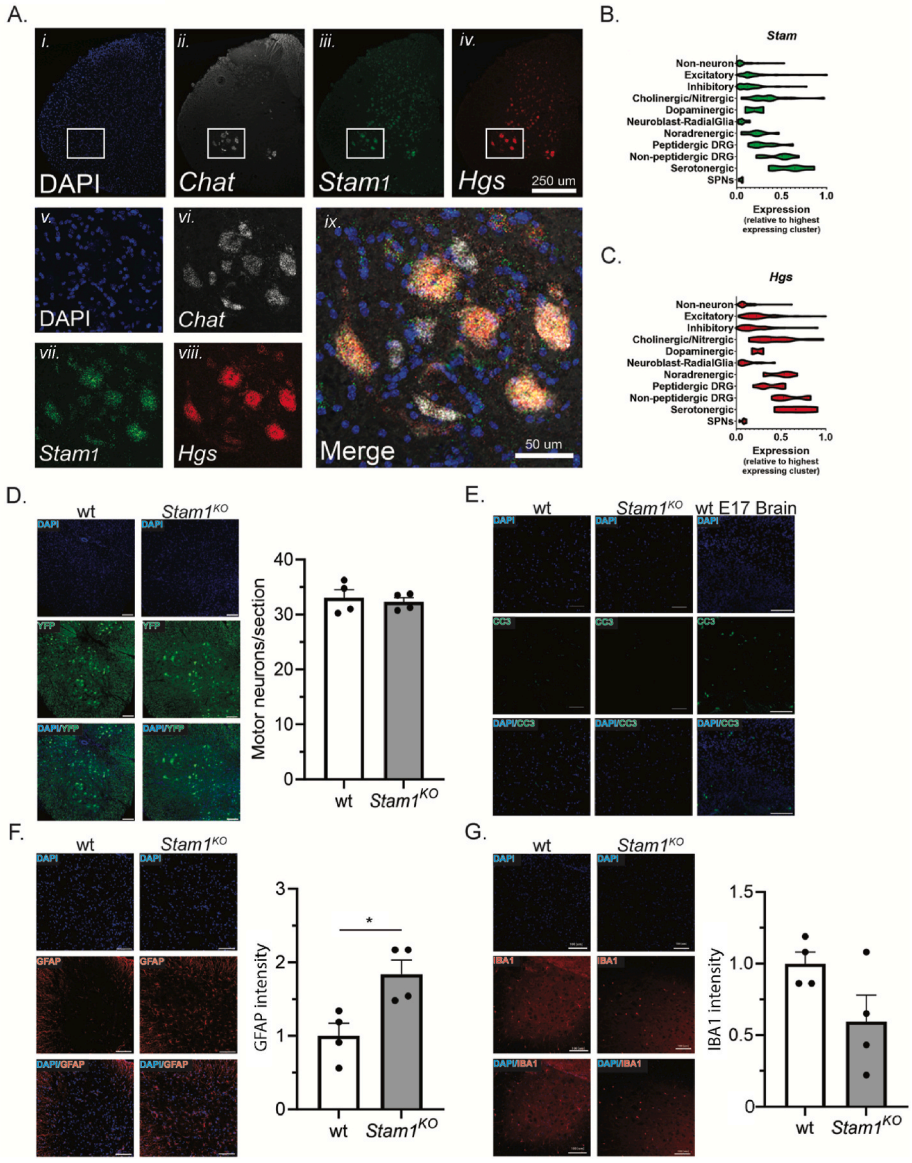

Fig. 2. Pathological analysis of *Stam1*^{KO} spinal cords. (A) Representative images of multi-plex fluorescent *in situ* hybridization for (*ii.)* choline acetyltransferase (*Chat*), (*iii.*) *Stam1*, and (*iv.*) *Hgs* mRNA in sections co-stained with (*i.*) DAPI. The boxed area is zoomed in to show expression of (*vi.*) *Chat*, (*vii.*) *Stam1* and (*viii.*) *Hgs* as well as (*v.*) DAPI in motor neurons. (*ix.*) Merged images of *Chat*, *Stam1*, *Hgs* and DAPI. Relative expression levels of (B) *Stam1* and (C) *Hgs* in different cell types in the mouse brain and spinal cord (from mousebrain.org). (D–G) Analysis of lumbar 4/5 spinal segment pathology in *Stam1*^{KO} mice. (D) Representative L4/5 spinal cord sections and quantitation of motor neurons ($p = 0.2802$) from spinal cords of 3-month-old wt and *Stam1*^{KO} mice containing the *Thy1-Yfp* transgene. Spinal cords from 3-month-old wt and *Stam1*^{KO} mice stained for DAPI and either (E) cleaved caspase 3 (CC3), (F) GFAP ($p = 0.017$), or (G) IBA1 ($p = 0.0929$). Since no CC3 positive cells were identified in either the 3-month-old wt or *Stam1*^{KO} spinal cords, brain sections from embryonic day 17 (E17) wt mice were included as a positive control for CC3 staining. *$p < 0.05$.

available data demonstrating *Hgs* and *Stam1* expression in multiple neuron types in the mouse brain and spinal cord (Fig. 2B and C).

To determine if deletion of *Stam1* was associated with a loss of motor neurons, we compared motor neuron numbers in the lumbar region from 3-month-old *Stam1*^{KO} and control mice that transgenically express the yellow fluorescent protein from the *Thy1* promoter (*Thy1-Yfp*), enabling visualization of the motor neurons in the ventral horn (Burgess et al., 2016). The number of motor neurons in the 3-month-old *Stam1*^{KO} mice was similar to that observed in the control mice (Fig. 2D). In addition, whereas cleaved caspase 3 staining could be easily detected in E17 positive control brain sections from wild-type mice, no actively degenerating, cleaved caspase 3-positive motor neurons were detected in the *Stam1*^{KO} mice (Fig. 2E). Taken together, these results suggest that deletion of STAM1 does not affect the survival of lower motor neurons.

Glial fibrillary acidic protein (GFAP) is an intermediate filament protein expressed in astrocytes and whose expression is often upregulated following CNS and PNS injury (Brenner, 2014). A recent study showed that neuronal loss of HGS, STAM1's ESCRT-0 binding partner, resulted in increased GFAP staining in the hippocampus (Lawrence et al., 2023). We also reported that GFAP expression was increased in the lumbar spinal cord region of HGS-deficient *teetering* mice (Watson et al., 2015). Here, we show that there was also a significant increase in GFAP staining in the lumbar spinal cords of 3-month-old *Stam1*^{KO} mice compared to controls (Fig. 2F). However, IBA1 staining was not significantly different in the spinal cords of the control and *Stam1*^{KO} mice (Fig. 2G), suggesting that loss of STAM1 was not sufficient to cause robust alterations in microglial recruitment or activation.

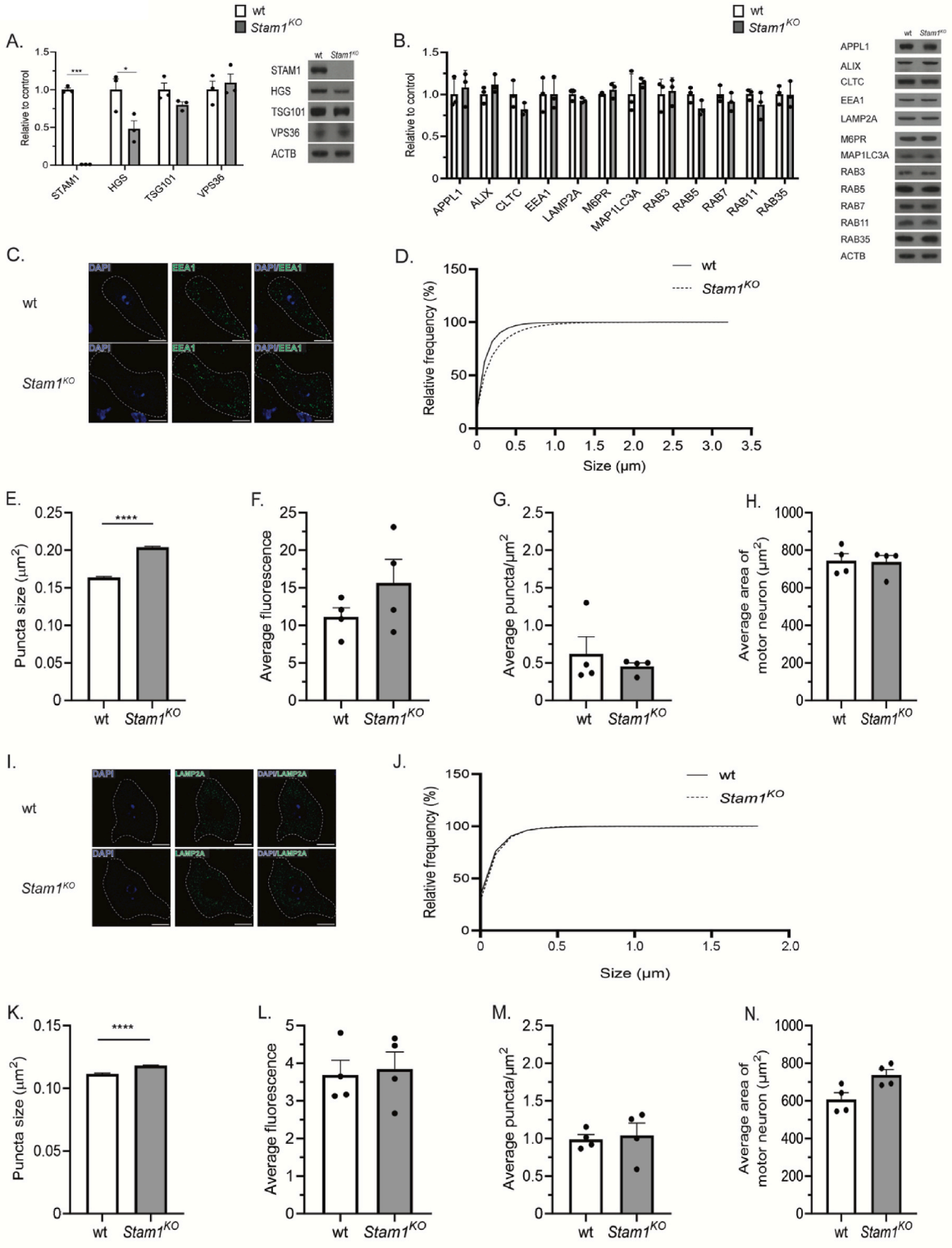

Fig. 3. Analysis of spinal cords from 3-month-old wild-type (wt) and *Stam1*^{KO} mice. Quantitation and representative immunoblots of (A) ESCRT proteins STAM1 ($p = 0.0001$), HGS ($p = 0.0352$), TSG101 ($p = 0.2422$), and VPS36 ($p = 0.6694$) and (B) endosomal proteins APPL1 ($p = 0.6239$), ALIX ($p = 0.9725$), CLTC ($p = 0.1518$), EEA1 ($p = 1.0$), LAMP2A ($p = 0.1688$), M6PR ($p = 0.3739$), MAP1LC3A ($p = 0.3951$), RAB3 ($p = 0.7899$), RAB5 ($p = 0.0926$), RAB7 ($p = 0.3506$), RAB11 ($p = 0.2578$) and RAB35 ($p = 0.953$). ACTB was used as a loading control. (C) L4/5 spinal cord segments from 3-month-old wt and *Stam1*^{KO} mice stained for EEA1 and DAPI. (D) Cumulative frequency plot showing the size distribution of EEA1 puncta in motor neurons from 3-month-old wt and *Stam1*^{KO} L4/5 spinal cord sections. The Kolmogorov-Smirnov test was used to determine significance. Average (E) size ($p < 0.00001$), (F) fluorescence intensity ($p = 0.2293$), and (G) number ($p = 0.5026$) of EEA1 puncta in 3-month-old wt and *Stam1*^{KO} mice. (H) Average area of motor neurons in 3-month-old wt and *Stam1*^{KO} mice ($p = 0.7429$). (I) L4/5 spinal cord segments from 3-month-old wt and *Stam1*^{KO} mice stained for LAMP2A and DAPI. (J) Cumulative frequency plot showing the size distribution of LAMP2A puncta in motor neurons from 3-month-old wt and *Stam1*^{KO} L4/5 spinal cord sections. The Kolmogorov-Smirnov test was used to determine significance. Average (K) size ($p < 0.00001$), (L) fluorescence intensity ($p = 0.8022$), and (M) number ($p = 0.777$) of LAMP2A puncta in 3-month-old wt and *Stam1*^{KO} mice. (N) Average area of motor neurons in 3-month-old wt and *Stam1*^{KO} mice ($p = 0.7609$). *$p < 0.05$, ****$p < 0.0001$.

3.3. Analysis of ESCRT and endosomal proteins in *Stam1*^{KO} mice

Our previous studies indicated that the levels of STAM1 were greatly reduced in the spinal cords of HGS-deficient *teetering* mice, suggesting that the association of STAM1 with HGS promotes its stability in the nervous system (Watson et al., 2015). This finding is consistent with *in vitro* studies showing that HGS is required for STAM1 stability in cell lines (Kobayashi et al., 2005). To determine if loss of STAM1 may also alter the expression of other components within the ESCRT pathway, we examined the levels of STAM1's ESCRT-0 binding partner, HGS, the ESCRT-I component TSG101, and the ESCRT-II component VPS36 in 3-month-old *Stam1*^{KO} and control mice. As expected, STAM1 was not detected in the spinal cords of the *Stam1*^{KO} mice (Fig. 3A). However, there was a 50% reduction in the levels of HGS in the spinal cords of the *Stam1*^{KO} mice, indicating that HGS is also destabilized in the absence of STAM1 (Fig. 3A). In contrast, there was no significant difference in the level of either TSG101 or VPS36 between the *Stam1*^{KO} and control mice (Fig. 3A), demonstrating that loss of STAM1 does not have a global effect on ESCRT protein levels in the spinal cord.

As *in vitro* experiments have shown that deficits in expression of HGS and STAM1 can influence the expression of other proteins within the endocytic pathway and alter the sorting of internalized cell surface cargo (Komada and Soriano, 1999; Marchese et al., 2003; Yan et al., 2005; Razi and Futter, 2006; Raiborg et al., 2008; Chanut-Delalande et al., 2010), we next examined if STAM1 deficiency altered the expression of proteins that localize to different endosomal compartments in the spinal cords of mice. No significant difference in the levels of markers for clathrin dependent endocytosis (CLTC), early endosomes (RAB5 and EEA1), recycling endosomes (RAB11), late endosomes (RAB7, LAMP2A and M6PR), the ESCRT adaptor protein ALIX, the endosomal adaptor protein APPL1, the vesicular transport protein RAB3, or the HGS-interacting protein RAB35 were observed in the spinal cord extracts of 3-month-old *Stam1*^{KO} mice compared to controls (Fig. 3B). Although ESCRTs have been suggested to regulate autophagy (Tamai et al., 2008; Takahashi et al., 2018; Zhen et al., 2020), there was also no significant difference in the level of the autophagy-related protein MAP1LC3A in the 3-month--old *Stam1*^{KO} mice compared to controls (Fig. 3B).

ESCRT components have been shown to have distinct roles in maintaining endosome structure, and depletion of HGS results in enlarged endosomes in cultured cells (Lloyd et al., 2002; Marchese et al., 2003; Razi and Futter, 2006). To investigate if loss of STAM1 also alters the structure of the endosome, we examined early (EEA1-positive) and late (LAMP2A-positive) endosomes in the L4/5 motor neurons of 3-month-old *Stam1*^{KO} mice and controls (Fig. 3C–N). Although there was no significant increase in the staining intensity or number of EEA1-positive puncta (Fig. 3F and G), there was a significant increase in the size of EEA1-positive puncta in the motor neurons of the *Stam1*^{KO} mice (Fig. 3D and E). Similar to what we observed for EEA1 staining, there was no significant change in the intensity or number of LAMP2-positive puncta (Fig. 3L and M), and there was an increase in the size of LAMP2A puncta in the *Stam1*^{KO} mice compared to controls (Fig. 3J and K). No significant difference was observed in the average size of the motor neurons between wild-type and *Stam1*^{KO} mice (Fig. 3H and N).

Since previous studies have demonstrated that alterations in the ESCRT-0 complexes disrupt the endosomal organization of critical factors required for the correct sorting of internalized cell surface cargo back to the cell surface or to the lysosome (Norris et al., 2017), we next examined the effect of STAM1 deficiency on the expression of several cell surface receptors and cytosolic proteins that are thought to be sorted to the lysosome by the ESCRT-0 complex (Marchese et al., 2003; Tamai et al., 2008; Huang et al., 2009; Chanut-Delalande et al., 2010; Sierra et al., 2010; Nam and Lee, 2016; McLean et al., 2022). Although loss of STAM1, and the subsequent loss of HGS (Fig. 3A), could be expected to alter the sorting of putative ESCRT-0 substrates to the lysosome for degradation, the levels of CXCR4, EGFR, ERBB2, ERBB4, GRIA1, and NTRK2 were not significantly different between the *Stam1*^{KO} mice and controls (Fig. 4A). However, there was a significant decrease in the level of the ERBB3 receptor in the spinal cord extracts from the 3-month-old *Stam1*^{KO} mice compared to controls (Fig. 4A), suggesting that the loss of STAM1 may result in the inappropriate targeting of ERBB3 to the lysosome for degradation. Since reduced ERBB3 expression was also observed in a mouse model of ALS, and increasing NRG1 levels was found to be neuroprotective in that model (Lasiene et al., 2016), this decrease in ERBB3 may also account for the neuromuscular defects in the *Stam1*^{KO} mice.

Previous *in vitro* studies have shown that STAMs are highly phosphorylated in response to growth factor stimulation and have implicated STAMs in cytokine signaling (Chanut-Delalande et al., 2010; Huang et al., 2010; Horner et al., 2018; Szymanska et al., 2018). However, loss of STAM1 did not appear to significantly alter the activation of downstream components of the AKT, ERK, GSK3β or JNK signaling pathways in the spinal cords of the 3-month-old *Stam1*^{KO} mice (Fig. 4B). In addition, when we examined the expression of several cytosolic aggregate-prone proteins that are believed to utilize the ESCRT pathway for lysosomal degradation (Oshima et al., 2016; Vaz-Silva et al., 2018; Chen et al., 2019; Lawrence et al., 2023), there was no difference in the steady-state levels of either PRNP, MAPT or TARDBP in the spinal cords of the *Stam1*^{KO} mice compared to controls (Fig. 4C). These findings suggest that the loss of STAM1 does not appear to result in the accumulation of these proteins in the spinal cords of *Stam1*^{KO} mice.

3.4. STAM1 is not required for sciatic nerve myelination

Our previous studies demonstrated that HGS deficiency blocked Schwann cell maturation and sciatic nerve myelination (McLean et al., 2022). To determine if STAM1 is also required for peripheral nerve myelination, we used transmission electron microscopy to compare the myelination profiles of the sciatic nerves from 3-month-old *Stam1*^{KO} and control mice (Fig. 5A). In the control mice, all of the large caliber axons (>1 μm in diameter) were myelinated by 3 months (Fig. 5A and B), which is consistent with what has previously been reported in rodents (Hahn et al., 1987). No significant differences were detected in either the percent of myelinated fibers, the g-ratio, or the axonal density (Fig. 5B–D) between the *Stam1*^{KO} and control sciatic nerves, suggesting that STAM1 is not essential for peripheral nerve myelination.

3.5. NMJ defects in *Stam1*^{KO} mice

Stam1^{KO} mice exhibit several signs of neuromuscular disease, including reduced muscle mass, grip strength and rotarod performance (Fig. 1). Since alterations in motor endplate structure were detected in the HGS-deficient *teetering* mice and are also observed in other models of neuromuscular disease (Fischer et al., 2004; Kong et al., 2009; Watson et al., 2015), we next compared NMJ innervation in the tibialis anterior muscles from *Stam1*^{KO} and control mice (Fig. 6A). Using *Stam1*^{KO} and wild-type control mice that transgenically express the yellow fluorescent protein in motor neurons and fluorescently-labeled α-bungarotoxin to identify AChR clusters on muscle fibers (Burgess et al., 2016), we found that almost all of the NMJs in the control mice were innervated by 1 month of age (Fig. 6B). Less than 2% of the NMJs in the control mice showed signs of swelling, and less than 5% exhibited terminal-sprouting (Fig. 6B and C). Although STAM1 deficiency did not cause a significant increase in NMJ denervation at one month, the NMJs from the 1-month--old *Stam1*^{KO} mice displayed significantly more terminal swellings and sproutings (Fig. 6B). The percentage of degenerating NMJs continued to increase and, by 3 months of age, the NMJs from the *Stam1*^{KO} mice showed significant signs of denervation, terminal swellings, and sproutings compared to controls (Fig. 6C). In addition, although there was no significant difference in the NMJ area defined by α-bungarotoxin staining between the *Stam1*^{KO} mice and controls at 1 month (Fig. 6D), the area of the NMJs was significantly decreased in the *Stam1*^{KO} mice at

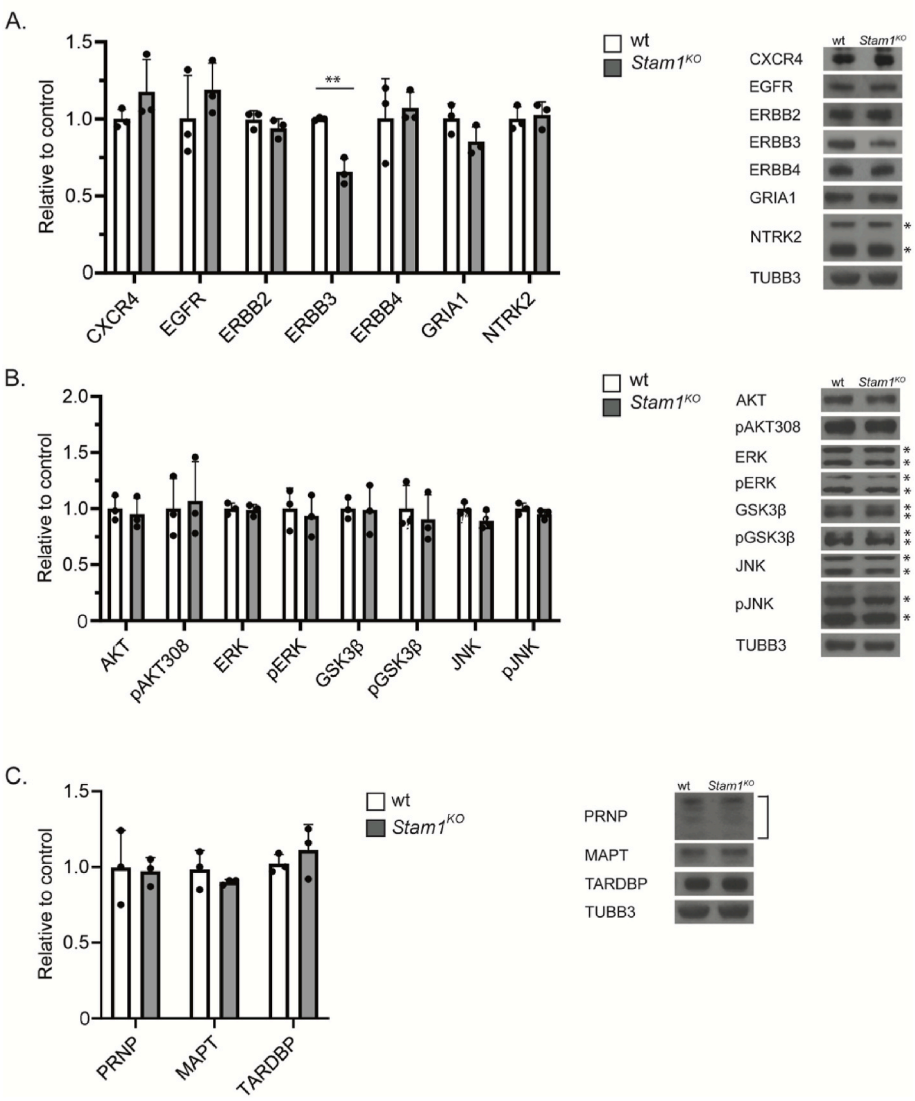

Fig. 4. Examination of ESCRT substrates and signaling pathways in spinal cords of *Stam1*^{KO} mice and controls. Quantitation and representative immunoblots of (A) the putative ESCRT substrates CXCR4 ($p = 0.2268$), EGFR ($p = 0.3782$), ERBB2 ($p = 0.3127$), ERBB3 ($p = 0.0025$), ERBB4 ($p = 0.6897$), GRIA1 ($p = 0.1423$) and NTRK2 ($p = 0.685$), (B) signaling molecules AKT ($p = 0.6817$), pAKT308 ($p = 0.8087$), ERK ($p = 0.8911$), pERK ($p = 0.6793$), GSK3β ($p = 0.9306$), pGSK3β ($p = 0.5961$), JNK ($p = 0.1324$) and pJNK ($p = 0.3227$), and (C) the aggregate-prone proteins PRNP ($p = 0.8684$), MAPT ($p = 0.3193$) and TARDBP ($p = 0.4392$) in spinal cord extracts of 3-month-old wild-type (wt) and *Stam1*^{KO} mice. When multiple known isoforms of a protein were detected, either an asterisk or bracket was placed next to the immunoblot to indicate bands that were quantitated. TUBB3 was used as a loading control. **$p < 0.01$.

3 months (Fig. 6E), suggesting that loss of STAM1 results in degeneration of the NMJs. No multiply innervated muscle fibers were observed in the *Stam1*^{KO} mice.

Since the *Stam1*^{KO} mice exhibited reduced muscle development, we next examined if loss of STAM1 affected the fiber size of the gastrocnemius muscles. While there was no significant difference at 1 month of age (Fig. 6F), there was a significant reduction in the cross-sectional area of the muscle fibers in the 3-month-old *Stam1*^{KO} mice compared to controls (Fig. 6G). As changes in connectivity between the muscle and nerve can alter muscle development and induce changes in the expression of the AChR subunits, we also compared AChR expression in 1- and 3-month-old *Stam1*^{KO} and control mice. qPCR analysis of the gastrocnemius AChR mRNAs demonstrated a significant increase in the level of the AChR-δ subunit in the *Stam1*^{KO} mice at both 1 and 3 months of age (Fig. 6H and I). Although no significant changes in the levels of the α, β, ε and γ AChR subunits were observed between the mice at 1 month of age, the levels of the ε and embryonic γ subunits were altered in the 3-month-old *Stam1*^{KO} mice compared to controls (Fig. 6I). Taken together, these results suggest that STAM1 is required to maintain proper NMJ structure, stability and function.

3.6. Loss of STAM1 leads to reduced levels of synaptic proteins

A previous *in vitro* study indicated that HGS is required for the degradation of a subset of synaptic vesicle proteins (Sheehan et al., 2016). Our findings of NMJ terminal swellings in both the *teetering* (Watson et al., 2015) and *Stam1*^{KO} mice suggests that loss of ESCRT-0 function may influence the degradation of synaptic proteins in these mouse models. To investigate this possibility, we used immunoblot analysis to examine the levels of several presynaptic proteins in spinal cord extracts from 3-month-old *Stam1*^{KO} and control mice. Although *Stam1* deficiency did not alter the levels of most of the proteins examined, there was a significant decrease in the levels of VAMP2 and VTI1A in the *Stam1*^{KO} mice compared to controls (Fig. 7A). As STAM1 deficiency had the most dramatic effect on VTI1A protein levels, we next compared the staining intensity for VTI1A in lumbar motor neurons

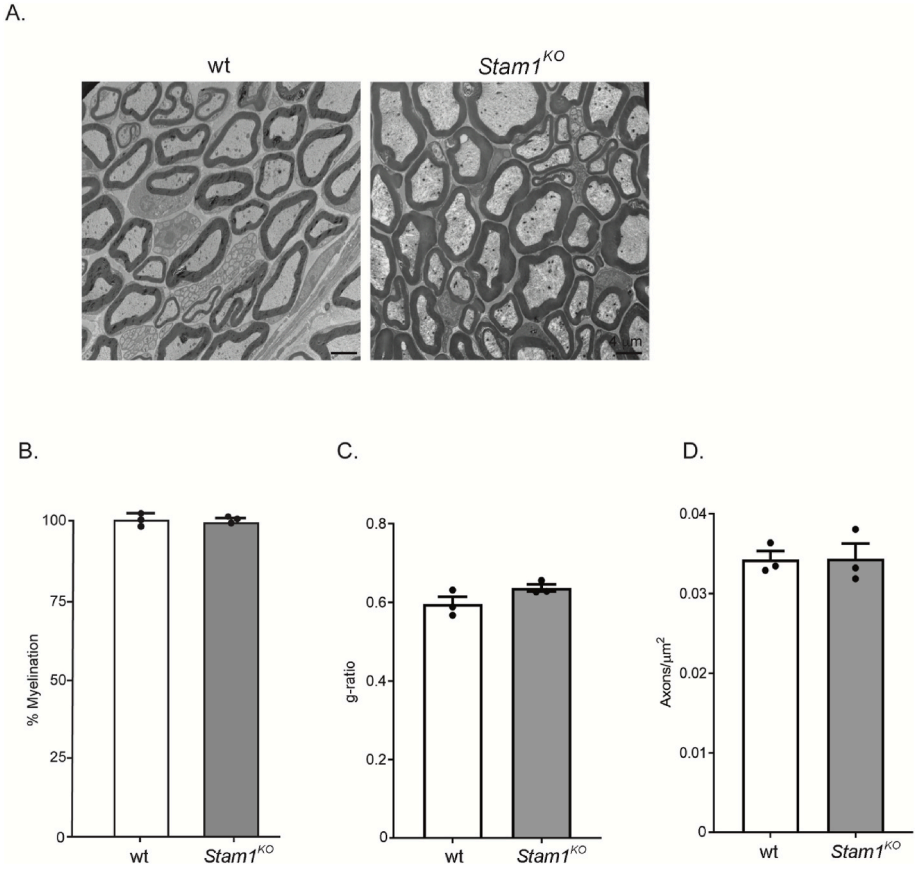

Fig. 5. STAM1 deficiency does not affect peripheral nerve myelination. (A) Representative electron micrographs of sciatic nerves from 3-month-old wild-type (wt) and *Stam1*^{KO} mice. Quantitation showing (B) the percent of sciatic nerve axons >1 μm in diameter that were myelinated ($p = 0.9286$), (C) the ratio of axon diameter to total nerve fiber thickness (g-ratio) ($p = 0.1205$), and (D) axon density ($p = 0.9541$) in sciatic nerves from wt and *Stam1*^{KO} mice.

from 3-month-old *Stam1*^{KO} and control mice. STAM1 deficiency resulted in a significant reduction in the size distribution of VTI1A puncta and in the intensity of VTI1A fluorescence in the motor neurons of the *Stam1*^{KO} mice compared to controls. (Fig. 7C–E). No significant difference was observed in the number of VTI1A puncta or the size of the motor neurons between the *Stam1*^{KO} and wild-type mice (Fig. 7F–G).

To investigate if STAM1 directly interacts with VTI1A, and could thus influence its endosomal sorting and stability, we next performed co-immunoprecipitation experiments on spinal cord extracts from 1-month-old wild-type mice. Spinal cord lysates were incubated with antibodies against STAM1, and the interacting protein complexes were retrieved with protein A/G magnetic beads. As expected, the STAM1 antibody efficiently isolated both STAM1 and its ESCRT-0 binding partner HGS from the spinal cord lysates (Fig. 7H). In contrast, we were unable to detect any interaction between VTI1A and STAM1 (Fig. 7H), which suggests that either STAM1 does not associate with VIT1A or that the interaction was not stable enough to detect by this assay.

4. Discussion

Deletion of STAM1 impaired muscle growth, strength, coordination and tactile sensitivity in *Stam1*^{KO} mice. These neuromuscular defects were not associated with motor neuron loss but did correlate with an increase in spinal cord gliosis. Although STAM1 deficiency did not have widespread effects on all endosomal proteins, this study demonstrated that, in addition to affecting the expression of its binding partner, HGS, loss of STAM1 also reduced the expression of the presynaptic SNARE proteins VAMP2 and VTI1A, implicating STAM1 in the stable sorting of Golgi cargo necessary for synaptic stability and function. The most profound defect observed in the *Stam1*^{KO} mice was the degeneration of NMJs that occurred as early as 1 month of age, suggesting that the neuromuscular disease in the *Stam1*^{KO} mice may initiate from a "dying-back" axonopathy, as is seen in other motor neuron diseases (Fischer et al., 2004).

We set out to investigate the effects of loss of STAM1, a component of the ESCRT-0 complex, on the neuromuscular system. Our previous studies demonstrated that HGS deficiency causes a motor and sensory neuropathy in mice that is associated with functional and structural changes at the NMJ (Watson et al., 2015). The *Stam1*^{KO} mice resembled several aspects of the HGS-deficient mice, including reduced neuromuscular strength, muscle atrophy, motor endplate degeneration, increased GFAP staining in the spinal cord (Watson et al., 2015), and altered expression of the ERBB3 receptor (McLean et al., 2022). However, unlike HGS deficiency, loss of STAM1 did not alter the myelination of the sciatic nerve, possibly due to compensation by STAM2 in Schwann cells (Yamada et al., 2002). Alternatively, the additional myelination defect in the *teetering* mice may indicate that HGS has a role in Schwann cell myelination that does not rely on its association with STAM1. However, our demonstration of motor endplate disease in both the *Stam1*^{KO} and *teetering* mice suggests that this neurological phenotype is due to deficits in the same endosomal pathway.

The ESCRT pathway has been shown to sort proteins through the endolysosomal pathway in order to maintain presynaptic protein homeostasis (Sheehan et al., 2016; Sheehan and Waites, 2019; Birdsall et al., 2022). In an activity-dependent manner, RAB35 recruits HGS to synaptic vesicles, and disruption of this interaction results in reduced degradation of VAMP2 and SV2 (Sheehan et al., 2016). Interestingly, RAB35 only weakly recruits STAM1 to synaptic vesicles following neuronal activity (Sheehan et al., 2016), which implied that STAM1 was not required for the correct sorting of VAMP2 and SV2. However, when

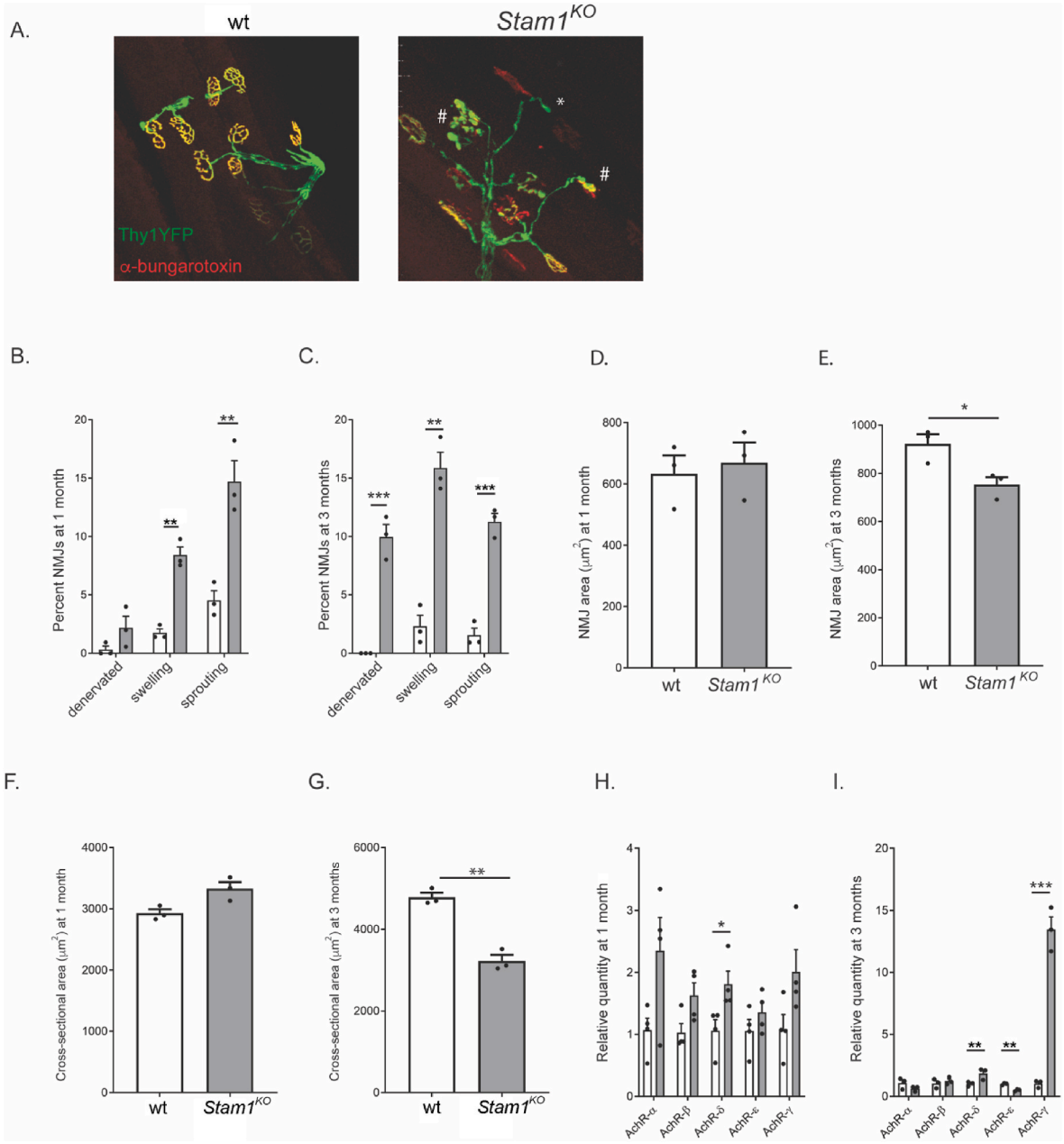

Fig. 6. STAM1 deletion causes NMJ and muscle defects in *Stam1*^{KO} mice. (A) Representative muscle fibers from tibialis anterior muscles of 3-month-old wild-type (wt) and *Stam1*^{KO} mice containing the *Thy1-Yfp* transgene were stained with TRITC-α-bungarotoxin (red) to label the postsynaptic AChRs. The presynaptic axons and terminals were visualized by fluorescence from the *Thy1-Yfp* transgene (green). # represents swollen terminals and * represents synaptic terminal sproutings in the *Stam1*^{KO} mice. Quantitation of NMJs from (B) 1-month-old or (C) 3-month-old wt and *Stam1*^{KO} mice that showed denervation (1 month $p = 0.1483$, 3 month $p = 0.0007$), swellings (1 month $p = 0.001$, 3 month $p = 0.0012$) or terminal sproutings (1 month $p = 0.0068$, 3 month $p = 0.0005$). Quantitation of NMJ area from (D) 1-month-old ($p = 0.7007$) and (E) 3-month-old ($p = 0.03$) wt and *Stam1*^{KO} mice. Quantitation of cross-sectional area from gastrocnemius muscles of (F) 1-month-old ($p = 0.0659$) and (G) 3-month-old ($p = 0.0011$) wt and *Stam1*^{KO} mice. qPCR analysis of AChR expression in gastrocnemius muscles of (H) 1-month-old and (I) 3-month-old wt or *Stam1*^{KO} mice (AChR-α: 1 month $p = 0.066$, 3 month $p = 0.2428$; AChR-β: 1 month $p = 0.055$, 3 month $p = 0.4802$; AChR-δ: 1 month $p = 0.0351$, 3 month $p = 0.00364$; AChR-ε: 1 month $p = 0.2638$, 3 month $p = 0.0036$; and AChR-γ: 1 month $p = 0.0788$, 3 month $p = 0.0002$). Open boxes indicate wt mice and grey boxes indicate *Stam1*^{KO} mice. *$p < 0.05$, **$p < 0.01$, ***$p < 0.001$. (For interpretation of the references to colour in this figure legend, the reader is referred to the Web version of this article.)

we compared the expression of several presynaptic proteins in spinal cord extracts from *Stam1*^{KO} mice and controls, loss of STAM1 resulted in a reduction in the levels of VAMP2 and VTI1A. Quantitation of VTI1A levels by immunofluorescence demonstrated an even greater reduction of VTI1A specifically in the motor neurons of *Stam1*^{KO} mice and suggests that STAM1 may sort VTI1A to the recycling endosome and prevent its degradation. Interestingly, loss of *Vti1a/b* in hippocampal neuronal cultures has been reported to result in reduced expression of several presynaptic proteins at synapses, including VAMP2 (Emperador-Melero et al., 2018), suggesting that the loss of VAMP2 in the *Stam1*^{KO} mice may be indirectly related to the loss of VTI1A. In addition, *in vivo* studies demonstrated severe neurodevelopmental abnormalities in *Vti1a/1b* double knockout mice, including degeneration of L2 lower motor neurons and impaired axonal growth (Kunwar et al., 2011), which supports a possible link between reduced VTI1A levels and motor endplate disease in the *Stam1*^{KO} mice. Additional studies are required to determine if

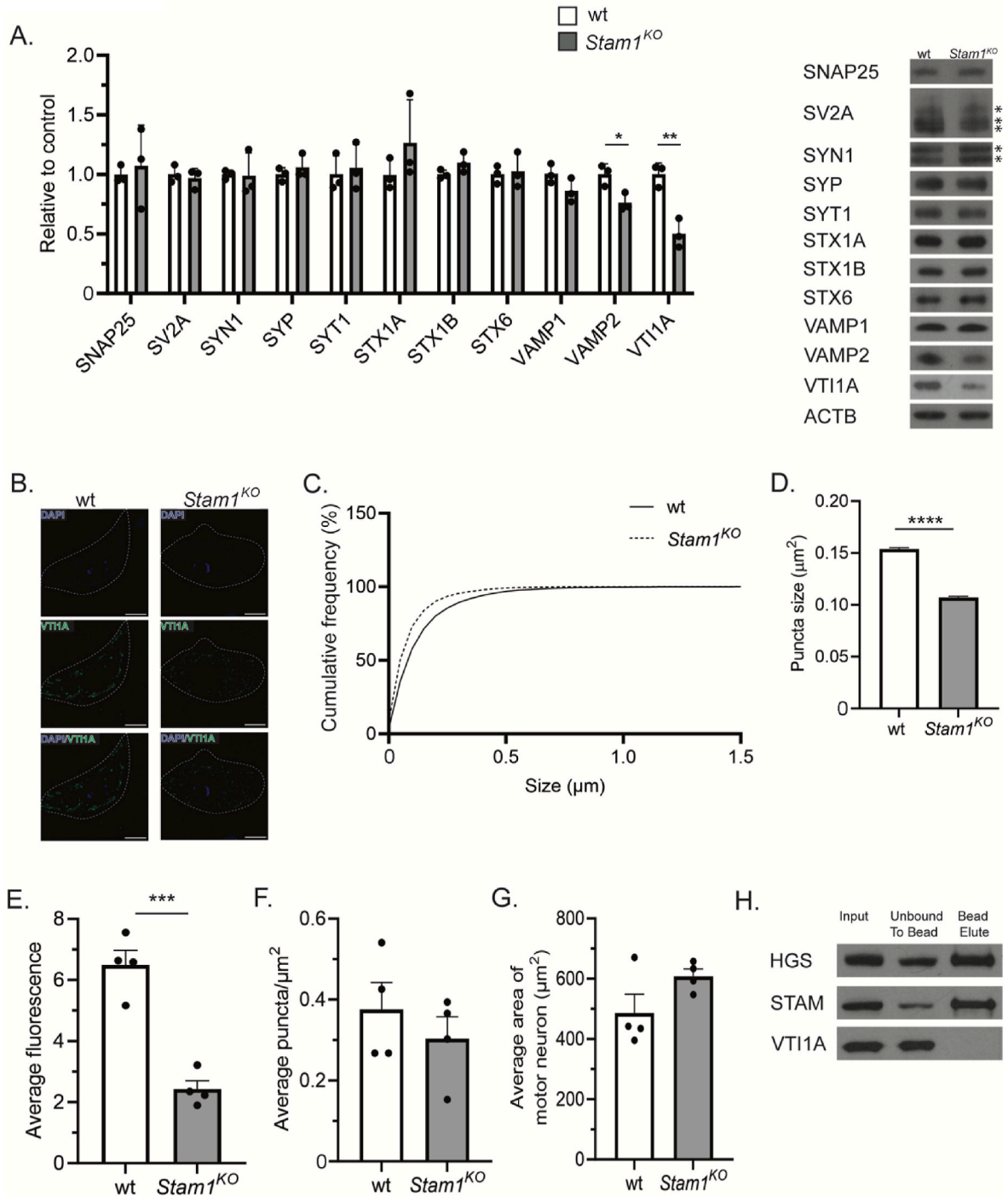

Fig. 7. STAM1 deletion causes reduced expression of VTI1A and VAMP2. (A) Quantitation and representative immunoblots showing levels of SNAP25 ($p = 0.7208$), SV2A ($p = 0.6292$), SYN1 ($p = 0.9335$), SYP ($p = 0.4278$), SYT1 ($p = 0.7787$), STX1A ($p = 0.2887$), STX1B ($p = 0.1477$), STX6 ($p = 0.7953$), VAMP1 ($p = 0.1282$), VAMP2 ($p = 0.0247$) and VTI1A ($p = 0.0049$) in the spinal cords of 3-month-old wild-type (wt) and *Stam1*^{KO} mice. When multiple known isoforms of a protein were detected, an asterisk was placed next to immunoblot to indicate the protein bands that were quantitated. ACTB was used as a loading control. (B) Representative L4/5 spinal cord segments from 3-month-old wt and *Stam1*^{KO} mice stained for VTI1A and DAPI. (C) Cumulative frequency plot showing the size distribution of VTI1A puncta in motor neurons of 3-month-old wt and *Stam1*^{KO} mice. The Kolmogorov-Smirnov test was used to determine significance. Quantitation of average (D) size ($p < 0.0001$), (E) fluorescence intensity ($p = 0.0004$) and (F) number ($p = 0.4337$) of VTI1A puncta in L4/5 spinal cord segments from 3-month-old wt and *Stam1*^{KO} mice. (G) Average area of motor neurons in 3-month-old wt and *Stam1*^{KO} mice ($p = 0.7609$). (H) Immunoblot analysis of proteins that co-immunoprecipitated with STAM1 in spinal cord lysates from 1-month-old wild-type mice. Lanes represent input lysate, proteins that did not bind to the beads, and proteins that were captured by the STAM1 antibody bead complex. *$p < 0.05$, **$p < 0.01$, ***$p < 0.001$, ****$p < 0.0001$.

Vti1a mRNA levels are reduced in the motor neurons of *Stam1*^{KO} mice, as that could also explain the reduction in VTI1A protein levels.

VTI1A is an endolysosomal Qb SNARE protein (Brandhorst et al., 2006) that localizes to both the Golgi apparatus and early endosomes (Brandhorst et al., 2006; Emperador-Melero et al., 2018). It is believed to function in neuronal secretion by modulating the sorting of secretory cargo and proteins into and away from the Golgi apparatus (Xu et al., 1998; Kreykenbohm et al., 2002; Ganley et al., 2008a; Hoopmann et al.,

2010; Emperador-Melero et al., 2018, 2019). VTI1A is also required for retrograde transport of M6PR from the endosome to the Golgi apparatus in embryonic fibroblasts and HeLa cells (Medigeshi and Schu, 2003; Ganley et al., 2008b). Our data indicated that the distribution of VTI1A in motor neuron cell bodies was predominantly at the Golgi apparatus. This is consistent with VTI1A playing a role in sorting secretory cargo and synaptic secretion machinery from the Golgi to the presynaptic terminal (Emperador-Melero et al., 2018). Since there did not appear to be any alterations in Golgi morphology in the motor neurons of the *Stam1*^{KO} mice, we speculate that loss of STAM1 and VTI1A expression causes a functional change in the ability of the Golgi to supply components of the neuronal secretory apparatus to the synapse, causing denervation, endplate swellings and sprouting at the NMJs of *Stam1*^{KO} mice. If STAM1 is also required for the retrograde transport of VTI1A from the endosome to the Golgi then, in the absence of STAM1, VTI1A may not be properly sorted back to the Golgi. Consistent with this idea, STAM proteins contain a 140 amino acid VHS domain that is found in proteins that are involved in endosomal trafficking and/or localize to the Golgi apparatus (Dell'Angelica et al., 2000; Wang et al., 2010). Previous reports utilizing HeLa cells demonstrated that STAM proteins colocalized with markers for both early endosomes and the Golgi, and showed that overexpression of either STAM1 or STAM2 resulted in Golgi fragmentation, suggesting that STAM proteins play a role in Golgi homeostasis (Rismanchi et al., 2009). In addition, ESCRT proteins have been shown to mediate protein and/or vesicle trafficking from the Golgi to endosomes/lysosomes (Hirota et al., 2021). While many endocytic proteins are found at multiple locations, it is unclear if the effects of STAM1 depletion on VTI1A levels indicate a requirement of STAM1 to sort VTI1A along the exocytic pathway or are secondary to STAM1 depletion on the endolysosomal pathway. Future experiments could explore if changes in trafficking of synaptic proteins occur prior to NMJ degeneration in the *Stam1*^{KO} mice.

Our studies demonstrate that STAM1 is essential for maintaining motor neuron connections at the NMJ. This finding supports previous studies demonstrating that, in flies, STAM1 is regulated by ISL1-LHX3 homeobox proteins in motor neurons and functions as a crucial regulator of ventral motor neuron axon pathfinding (Nam and Lee, 2016). We found STAM1 deletion causes a progressive decrease in muscle fiber size, elevated AChR-γ expression, and increased motor-endplate pathology which is similar to that observed in ALS patients (Bjornskov et al., 1984; Tsujihata et al., 1984; Palma et al., 2016). These results support a role for STAM1 in the stability of axonal connections in mammalian motor neurons. With the known requirement of VTI1A in the development of axonal projections in mice, and VTI1A's ability to modulate exocytosis of synaptic vesicles and dense core vesicles, we suggest that STAM1 plays an important role in regulating the level of VTI1A, and likely other presynaptic proteins, that are collectively required for maintaining motor endplate function.

Funding

This research was supported by the National Institute of Health/National Institute of Neurological Disorders and Stroke (R01 NS110744 to S.M.W.).

CRediT authorship contribution statement

John W. McLean: data processing, imaging, writing, revisions. **Mary VanHart:** data processing, imaging, writing. **Madilyn P. McWilliams:** imaging. **Charlene B. Farmer:** Technical assistance. **David K. Crossman:** data processing. **Rita M. Cowell:** imaging, writing, revisions. **Julie A. Wilson:** writing, revisions. **Scott M. Wilson:** writing, revisions.

Declaration of competing interest

The authors declare that they have no known competing financial interests or personal relationships that could have appeared to influence the work reported in this paper.

Data availability

No data was used for the research described in the article.

References

Babst, M., 2005. A protein's final ESCRT. Traffic 6, 2–9.
Bilodeau, P.S., Urbanowski, J.L., Winistorfer, S.C., Piper, R.C., 2002. The Vps27p Hse1p complex binds ubiquitin and mediates endosomal protein sorting. Nat. Cell Biol. 4, 534–539.
Birdsall, V., Kirwan, K., Zhu, M., Imoto, Y., Wilson, S.M., Watanabe, S., Waites, C.L., 2022. Axonal transport of Hrs is activity dependent and facilitates synaptic vesicle protein degradation. Life Sci. Alliance 5.
Bjornskov, E.K., Norris Jr., F.H., Mower-Kuby, J., 1984. Quantitative axon terminal and end-plate morphology in amyotrophic lateral sclerosis. Arch. Neurol. 41, 527–530.
Brandhorst, D., Zwilling, D., Rizzoli, S.O., Lippert, U., Lang, T., Jahn, R., 2006. Homotypic fusion of early endosomes: SNAREs do not determine fusion specificity. P Natl Acad Sci USA 103, 2701–2706.
Brenner, M., 2014. Role of GFAP in CNS injuries. Neurosci. Lett. 565, 7–13.
Burgess, R.W., Cox, G.A., Seburn, K.L., 2016. Neuromuscular disease models and analysis. Methods Mol. Biol. 1438, 349–394.
Chanut-Delalande, H., Jung, A.C., Baer, M.M., Lin, L., Payre, F., Affolter, M., 2010. The hrs/stam complex acts as a positive and negative regulator of RTK signaling during Drosophila development. PLoS One 5.
Chen, J.J., Nathaniel, D.L., Raghavan, P., Nelson, M., Tian, R., Tse, E., Hong, J.Y., See, S. K., Mok, S.A., Hein, M.Y., Southworth, D.R., Grinberg, L.T., Gestwicki, J.E., Leonetti, M.D., Kampmann, M., 2019. Compromised function of the ESCRT pathway promotes endolysosomal escape of tau seeds and propagation of tau aggregation. J. Biol. Chem. 294, 18952–18966.
Chen, P.C., Qin, L.N., Li, X.M., Walters, B.J., Wilson, J.A., Mei, L., Wilson, S.M., 2009. The proteasome-associated deubiquitinating enzyme Usp14 is essential for the maintenance of synaptic ubiquitin levels and the development of neuromuscular junctions. J. Neurosci. 29, 10909–10919.
Dell'Angelica, E.C., Puertollano, R., Mullins, C., Aguilar, R.C., Vargas, J.D., Hartnell, L. M., Bonifacino, J.S., 2000. GGAs: a family of ADP ribosylation factor-binding proteins related to adaptors and associated with the Golgi complex. J. Cell Biol. 149, 81–94.
Diab, R., Pilotto, F., Saxena, S., 2023. Autophagy and neurodegeneration: unraveling the role of C9ORF72 in the regulation of autophagy and its relationship to ALS-FTD pathology. Front. Cell. Neurosci. 17, 1086895.
Emperador-Melero, J., Toonen, R.F., Verhage, M., 2019. Vti proteins: beyond endolysosomal trafficking. Neuroscience 420, 32–40.
Emperador-Melero, J., Huson, V., van Weering, J., Bollmann, C., von Mollard, G.F., Toonen, R.F., Verhage, M., 2018. Vti1a/b regulate synaptic vesicle and dense core vesicle secretion via protein sorting at the Golgi. Nat. Commun. 9.
Fischer, L.R., Culver, D.G., Tennant, P., Davis, A.A., Wang, M.S., Castellano-Sanchez, A., Khan, J., Polak, M.A., Glass, J.D., 2004. Amyotrophic lateral sclerosis is a distal axonopathy: evidence in mice and man. Exp. Neurol. 185, 232–240.
Ganley, I.G., Espinosa, E., Pfeffer, S.R., 2008a. A syntaxin 10-SNARE complex distinguishes two distinct transport routes from endosomes to the trans-Golgi in human cells. JCB (J. Cell Biol.) 180, 159–172.
Ganley, I.G., Espinosa, E., Pfeffer, S.R., 2008b. A syntaxin 10-SNARE complex distinguishes two distinct transport routes from endosomes to the trans-Golgi in human cells. J. Cell Biol. 180, 159–172.
Hahn, A.F., Chang, Y., Webster, H.D., 1987. Development of myelinated nerve fibers in the sixth cranial nerve of the rat: a quantitative electron microscope study. J. Comp. Neurol. 260, 491–500.
Hirota, Y., Hayashi, M., Miyauchi, Y., Ishii, Y., Tanaka, Y., Fujimoto, K., 2021. LAPTM4 alpha is targeted from the Golgi to late endosomes lysosomes in a manner dependent on the E3 ubiquitin ligase Nedd4-1 and ESCRT proteins. Biochem Bioph Res Co 556, 9–15.
Hoopmann, P., Punge, A., Barysch, S.V., Westphal, V., Buckers, J., Opazo, F., Bethani, I., Lauterbach, M.A., Hell, S.W., Rizzoli, S.O., 2010. Endosomal sorting of readily releasable synaptic vesicles. Proc. Natl. Acad. Sci. U.S.A. 107, 19055–19060.
Horner, D.S., Pasini, M.E., Beltrame, M., Mastrodonato, V., Morelli, E., Vaccari, T., 2018. ESCRT genes and regulation of developmental signaling. Semin. Cell Dev. Biol. 74, 29–39.
Huang, H.R., Chen, Z.J.J., Kunes, S., Chang, G.D., Maniatis, T., 2010. Endocytic pathway is required for Drosophila Toll innate immune signaling. P Natl Acad Sci USA 107, 8322–8327.
Huang, S.H., Zhao, L., Sun, Z.P., Li, X.Z., Geng, Z., Zhang, K.D., Chao, M.V., Chen, Z.Y., 2009. Essential role of hrs in endocytic recycling of full-length TrkB receptor but not its isoform TrkB. T1. Journal of Biological Chemistry 284, 15126–15136.
Hurley, J.H., 2008. ESCRT complexes and the biogenesis of multivesicular bodies. Curr. Opin. Cell Biol. 20, 4–11.

Jackson, M.P., Hewitt, E.W., 2016. Cellular proteostasis: degradation of misfolded proteins by lysosomes. Essays Biochem. 60, 173–180.
Kobayashi, H., Tanaka, N., Asao, H., Miura, S., Kyuuma, M., Semura, K., Ishii, N., Sugamura, K., 2005. Hrs, a mammalian master molecule in vesicular transport and protein sorting, suppresses the degradation of ESCRT proteins signal transducing adaptor molecule 1 and 2. J. Biol. Chem. 280, 10468–10477.
Komada, M., Soriano, P., 1999. Hrs, a FYVE finger protein localized to early endosomes, is implicated in vesicular traffic and required for ventral folding morphogenesis. Gene Dev. 13, 1475–1485.
Kong, L.L., Wang, X.Y., Choe, D.W., Polley, M., Burnett, B.G., Bosch-Marce, M., Griffin, J. W., Rich, M.M., Sumner, C.J., 2009. Impaired synaptic vesicle release and immaturity of neuromuscular junctions in spinal muscular atrophy mice. J. Neurosci. 29, 842–851.
Kreykenbohm, V., Wenzel, D., Antonin, W., Atlachkine, V., von Mollard, G.F., 2002. The SNAREs vti1a and vti1b have distinct localization and SNARE complex partners. Eur. J. Cell Biol. 81, 273–280.
Kunwar, A.J., Rickmann, M., Backofen, B., Browski, S.M., Rosenbusch, J., Schoning, S., Fleischmann, T., Krieglstein, K., Fischer von Mollard, G., 2011. Lack of the endosomal SNAREs vti1a and vti1b led to significant impairments in neuronal development. Proc. Natl. Acad. Sci. U.S.A. 108, 2575–2580.
Lasiene, J., Komine, O., Fujimori-Tonou, N., Powers, B., Endo, F., Watanabe, S., Shijie, J., Ravits, J., Horner, P., Misawa, H., Yamanaka, K., 2016. Neuregulin 1 confers neuroprotection in SOD1-linked amyotrophic lateral sclerosis mice via restoration of C-boutons of spinal motor neurons. Acta Neuropathol Commun 4, 15.
Lawrence, J.A., et al., 2023. Diminished neuronal ESCRT-0 function exacerbates AMPA receptor derangement and accelerates prion-induced neurodegeneration. J. Neurosci.
Lloyd, T.E., Atkinson, R., Wu, M.N., Zhou, Y., Pennetta, G., Bellen, H.J., 2002. Hrs regulates endosome membrane invagination and tyrosine kinase receptor signaling in Drosophila. Cell 108, 261–269.
Marchese, A., Raiborg, C., Santini, F., Keen, J.H., Stenmark, H., Benovic, J.L., 2003. The E3 ubiquitin ligase AIP4 mediates ubiquitination and sorting of the G protein-coupled receptor CXCR4. Dev. Cell 5, 709–722.
McLean, J.W., Wilson, J.A., Tian, T., Watson, J.A., VanHart, M., Bean, A.J., Scherer, S.S., Crossman, D.K., Ubogu, E., Wilson, S.M., 2022. Disruption of endosomal sorting in Schwann cells leads to defective myelination and endosomal abnormalities observed in charcot-marie-tooth disease. J. Neurosci. 42, 5085–5101.
Medigeshi, G.R., Schu, P., 2003. Characterization of the in vitro retrograde transport of MPR46. Traffic 4, 802–811.
Nam, H., Lee, S., 2016. Identification of STAM1 as a novel effector of ventral projection of spinal motor neurons. Development 143, 2334–2343.
Norris, A., Tammineni, P., Wang, S., Gerdes, J., Murr, A., Kwan, K.Y., Cai, Q., Grant, B.D., 2017. SNX-1 and RME-8 oppose the assembly of HGRS-1/ESCRT-0 degradative microdomains on endosomes. Proc. Natl. Acad. Sci. U.S.A. 114, E307–E316.
O'Reilly, J., Ono-Moore, K.D., Chintapalli, S.V., Rutkowsky, J.M., Tolentino, T., Lloyd, K. C.K., Olfert, I.M., Adams, S.H., 2021. Sex differences in skeletal muscle revealed through fiber type, capillarity, and transcriptomics profiling in mice. Phys. Rep. 9.
Oshima, R., Hasegawa, T., Tamai, K., Sugeno, N., Yoshida, S., Kobayashi, J., Kikuchi, A., Baba, T., Futatsugi, A., Sato, I., Satoh, K., Takeda, A., Aoki, M., Tanaka, N., 2016. ESCRT-0 dysfunction compromises autophagic degradation of protein aggregates and facilitates ER stress-mediated neurodegeneration via apoptotic and necroptotic pathways. Sci. Rep. 6, 24997.
Palma, E., Reyes-Ruiz, J.M., Lopergolo, D., Roseti, C., Bertollini, C., Ruffolo, G., Cifelli, P., Onesti, E., Limatola, C., Miledi, R., Inghilleri, M., 2016. Acetylcholine receptors from human muscle as pharmacological targets for ALS therapy. P Natl Acad Sci USA 113, 3060–3065.
Parkinson, N., Ince, P.G., Smith, M.O., Highley, R., Skibinski, G., Andersen, P.M., Morrison, K.E., Pall, H.S., Hardiman, O., Collinge, J., Shaw, P.J., Fisher, E.M., Study, M., Consortium, F.R., 2006. ALS phenotypes with mutations in CHMP2B (charged multivesicular body protein 2B). Neurology 67, 1074–1077.
Puls, I., Jonnakuty, C., LaMonte, B.H., Holzbaur, E.L., Tokito, M., Mann, E., Floeter, M.K., Bidus, K., Drayna, D., Oh, S.J., Brown Jr., R.H., Ludlow, C.L., Fischbeck, K.H., 2003. Mutant dynactin in motor neuron disease. Nat. Genet. 33, 455–456.
Raiborg, C., Malerod, L., Pedersen, N.M., Stenmark, H., 2008. Differential functions of Hrs and ESCRT proteins in endocytic membrane trafficking. Exp. Cell Res. 314, 801–813.
Razi, M., Futter, C.E., 2006. Distinct roles for Tsg101 and Hrs in multivesicular body formation and inward vesiculation. Mol. Biol. Cell 17, 3469–3483.
Ripps, M.E., Huntley, G.W., Hof, P.R., Morrison, J.H., Gordon, J.W., 1995. Transgenic mice expressing an altered murine superoxide dismutase gene provide an animal model of amyotrophic lateral sclerosis. Proc. Natl. Acad. Sci. U.S.A. 92, 689–693.
Rismanchi, N., Puertollano, R., Blackstone, C., 2009. STAM adaptor proteins interact with COPII complexes and function in ER-to-Golgi trafficking. Traffic 10, 201–217.
Rusten, T.E., Vaccari, T., Stenmark, H., 2011. Shaping development with ESCRTs. Nat. Cell Biol. 14, 38–45.
Schreij, A.M., Fon, E.A., McPherson, P.S., 2016. Endocytic membrane trafficking and neurodegenerative disease. Cell. Mol. Life Sci. 73, 1529–1545.
Sheehan, P., Waites, C.L., 2019. Coordination of synaptic vesicle trafficking and turnover by the Rab35 signaling network. Small GTPases 10, 54–63.
Sheehan, P., Zhu, M., Beskow, A., Vollmer, C., Waites, C.L., 2016. Activity-dependent degradation of synaptic vesicle proteins requires Rab35 and the ESCRT pathway. J. Neurosci. 36, 8668–8686.
Sierra, M.I., Wright, M.H., Nash, P.D., 2010. AMSH interacts with ESCRT-0 to regulate the stability and trafficking of CXCR4. J. Biol. Chem. 285, 13990–14004.
Skibinski, G., Parkinson, N.J., Brown, J.M., Chakrabarti, L., Lloyd, S.L., Hummerich, H., Nielsen, J.E., Hodges, J.R., Spillantini, M.G., Thusgaard, T., Brandner, S., Brun, A., Rossor, M.N., Gade, A., Johannsen, P., Sorensen, S.A., Gydesen, S., Fisher, E.M., Collinge, J., 2005. Mutations in the endosomal ESCRTIII-complex subunit CHMP2B in frontotemporal dementia. Nat. Genet. 37, 806–808.
Smith, J.K., Mellick, G.D., Sykes, A.M., 2022. The role of the endolysosomal pathway in alpha-synuclein pathogenesis in Parkinson's disease. Front. Cell. Neurosci. 16, 1081426.
Szymanska, E., Budick-Harmelin, N., Miaczynska, M., 2018. Endosomal "sort" of signaling control: the role of ESCRT machinery in regulation of receptor-mediated signaling pathways. Semin. Cell Dev. Biol. 74, 11–20.
Takahashi, Y., He, H.Y., Tang, Z.Y., Hattori, T., Liu, Y., Young, M.M., Serfass, J.M., Chen, L.G., Gebru, M., Chen, C., Wills, C.A., Atkinson, J.M., Chen, H., Abraham, T., Wang, H.G., 2018. An autophagy assay reveals the ESCRT-III component CHMP2A as a regulator of phagophore closure. Nat. Commun. 9.
Tamai, K., Toyoshima, M., Tanaka, N., Yamamoto, N., Owada, Y., Kiyonari, H., Murata, K., Ueno, Y., Ono, M., Shimosegawa, T., Yaegashi, N., Watanabe, M., Sugamura, K., 2008. Loss of hrs in the central nervous system causes accumulation of ubiquitinated proteins and neurodegeneration. Am. J. Pathol. 173, 1806–1817.
Toupenet Marchesi, L., Leblanc, M., Stevanin, G., 2021. Current knowledge of endolysosomal and autophagy defects in hereditary spastic paraplegia. Cells-Basel 10.
Tsao, C.H., Wu, K.Y., Su, N.C., Edwards, A., Huang, G.J., 2023. The influence of sex difference on behavior and adult hippocampal neurogenesis in C57BL/6 mice. Sci Rep-Uk 13.
Tseng, C.S., Chao, Y.W., Liu, Y.H., Huang, Y.S., Chao, H.W., 2023. Dysregulated proteostasis network in neuronal diseases. Front. Cell Dev. Biol. 11, 1075215.
Tsujihata, M., Hazama, R., Yoshimura, T., Satoh, A., Mori, M., Nagataki, S., 1984. The motor end-plate fine structure and ultrastructural localization of acetylcholine receptors in amyotrophic lateral sclerosis. Muscle Nerve 7, 243–249.
Uytterhoeven, V., Kuenen, S., Kasprowicz, J., Miskiewicz, K., Verstreken, P., 2011. Loss of skywalker reveals synaptic endosomes as sorting stations for synaptic vesicle proteins. Cell 145, 117–132.
Vaz-Silva, J., Gomes, P., Jin, Q., Zhu, M., Zhuravleva, V., Quintremil, S., Meira, T., Silva, J., Dioli, C., Soares-Cunha, C., Daskalakis, N.P., Sousa, N., Sotiropoulos, I., Waites, C.L., 2018. Endolysosomal degradation of Tau and its role in glucocorticoid-driven hippocampal malfunction. EMBO J. 37.
Wang, C., Yue, F., Kuang, S., 2017. Muscle histology characterization using H&E staining and muscle fiber type classification using immunofluorescence staining. Bio Protoc 7.
Wang, T., Liu, N.S., Seet, L.F., Hong, W., 2010. The emerging role of VHS domain-containing Tom1, Tom1L1 and Tom1L2 in membrane trafficking. Traffic 11, 1119–1128.
Watson, J.A., Bhattacharyya, B.J., Vaden, J.H., Wilson, J.A., Icyuz, M., Howard, A.D., Phillips, E., DeSilva, T.M., Siegal, G.P., Bean, A.J., King, G.D., Phillips, S.E., Miller, R. J., Wilson, S.M., 2015. Motor and sensory deficits in the teetering mice result from mutation of the ESCRT component HGS. PLoS Genet. 11.
Wilson, S.M., Bhattacharyya, B., Rachel, R.A., Coppola, V., Tessarollo, L., Householder, D.B., Fletcher, C.F., Miller, R.J., Copeland, N.G., Jenkins, N.A., 2002. Synaptic defects in ataxia mice result from a mutation in Usp14, encoding a ubiquitin-specific protease. Nat. Genet. 32, 420–425.
Xu, Y., Wong, S.H., Tang, B.L., Subramaniam, V.N., Zhang, T., Hong, W., 1998. A 29-kilodalton Golgi soluble N-ethylmaleimide-sensitive factor attachment protein receptor (Vti1-rp2) implicated in protein trafficking in the secretory pathway. J. Biol. Chem. 273, 21783–21789.
Yamada, M., Ishii, N., Asao, H., Murata, K., Kanazawa, C., Sasaki, H., Sugamura, K., 2002. Signal-transducing adaptor molecules STAM1 and STAM2 are required for T-cell development and survival. Mol. Cell Biol. 22, 8648–8658.
Yamada, M., Takeshita, T., Miura, S., Murata, K., Kimura, Y., Ishii, N., Nose, M., Sakagami, H., Kondo, H., Tashiro, F., Miyazaki, J.I., Sasaki, H., Sugamura, K., 2001. Loss of hippocampal CA3 pyramidal neurons in mice lacking STAM1. Mol. Cell Biol. 21, 3807–3819.
Yan, Q., Sun, W., Kujala, P., Lotfi, Y., Vida, T.A., Bean, A.J., 2005. CART: an Hrs/actinin-4/BERP/myosin V protein complex required for efficient receptor recycling. Mol. Biol. Cell 16, 2470–2482.
Zeisek, A, Hochgerner, H, Lonnerberg, P, Johnsson, A, Memic, F, van der Zwan, J, Haring, M, Braun, E, Borm, LE, La Manno, Codeluppi, S, Furlan, A, Lee, K, Skene, N, Hjerling-Leffler, J, Arenas, E, Ernfors, P, Marklund, U, Linnarsson, S, 2018. Molecular Architecture of the Mouse Nervous System. Cell 174, 999–1014 e1022.
Zhen, Y., Spangenberg, H., Munson, M.J., Brech, A., Schink, K.O., Tan, K.W., Sorensen, V., Wenzel, E.M., Radulovic, M., Engedal, N., Simonsen, A., Raiborg, C., Stenmark, H., 2020. ESCRT-mediated phagophore sealing during mitophagy. Autophagy 16, 826–841.